

NUMERICAL SIMULATIONS OF A JET-CLOUD COLLISION AND STARBURST: APPLICATION TO MINKOWSKI'S OBJECT

P. CHRIS FRAGILE

Department of Physics & Astronomy, College of Charleston, Charleston, SC 29424, USA

PETER ANNINOS

Lawrence Livermore National Laboratory, Livermore, CA 94550, USA

STEVE CROFT

Astronomy Department, University of California, Berkeley, B-20 Hearst Field Annex #3411, Berkeley, CA 94720, USA

MARK LACY

National Radio Astronomy Observatory, 520 Edgemont Road, Charlottesville, VA 22903, USA

JASON W. L. WITRY

Department of Physics & Astronomy, College of Charleston, Charleston, SC 29424, USA

ABSTRACT

We present results of two- and three-dimensional, multi-physics simulations of an AGN jet colliding with an intergalactic cloud. The purpose of these simulations is to assess the degree of “positive feedback,” i.e. jet-induced star formation, that results from such a collision. We have specifically tailored our simulation parameters to facilitate comparison with recent observations of Minkowski's Object (M.O.), a stellar nursery located at the termination point of a radio jet coming from galaxy NGC 541. As shown in our simulations, such a collision triggers shocks which propagate around and through the cloud. These shocks condense the gas and trigger cooling instabilities, creating runaway increases in density, to the point that individual clumps can become Jeans unstable. Our simulations provide information about the expected star formation rate, total mass converted to H I, H₂, and stars, and the relative velocity of the stars and gas. Our results confirm the possibility of jet-induced star formation, though fail to match the level observed in M.O. We discuss ways in which the agreement might be improved in future simulations.

Keywords: galaxies: individual (Minkowski's Object) — galaxies: jets — hydrodynamics — intergalactic medium — shock waves

1. INTRODUCTION

The interaction between high-energy jets from active galactic nuclei (AGN) and their surroundings has long been a topic of great astrophysical interest. It is well known that AGN feedback can control the size of a galaxy by influencing star formation, but the mechanism behind this is not well understood. Several recent observations (Nesvadba et al. 2010; Guillard et al. 2015), as well as numerical studies (e.g. Sutherland & Bicknell 2007; Antonuccio-Delogu & Silk 2008; Gaibler et al. 2012), have demonstrated that AGN feedback can be “negative” or “positive.”

The exact astrophysical conditions in the jet and cloud are important in determining what direction feedback takes. Jets can be roughly divided according to their Fanaroff-Riley classification (Fanaroff & Riley 1974). Fast, energetic FR II jets seem more likely to result in negative feedback. Negative feedback curbs or even halts star formation, and is thought to result from the extreme radiative and kinetic energies of the jet, which heat and disperse the star-forming gas. Additionally, the kinetic energy of a jet creates turbulence that can prevent ambient gas from cooling and subsequently coalescing (e.g. Nesvadba et al. 2010). For example, a study of the system 3C 326 by Ogle et al. (2007) found that, despite the strong H₂ line emission and an inferred molecular gas mass of $2 \times 10^9 M_{\odot}$, the star formation is 20 times lower than predicted by the Kennicutt-Schmidt law. They infer that turbulent heating from the

jet is inhibiting star formation. Other studies, though, suggest increased star formation may be seen in the cocoon of such jets (e.g. Gaibler et al. 2012).

In contrast, FRI jets propagate through the ISM/IGM with energies high enough to create compression in the surrounding gas, but low enough to reduce the chance of significant turbulent heating. These jets are observed in positive feedback cases, wherein the effect of the jet serves to enhance star formation, including Centaurus A (Salomé et al. 2016, and references therein), 4C 41.17 (Bicknell et al. 2000), and Minkowski’s Object (hereafter M.O.) (Croft et al. 2006, hereafter C06). We give more details on both positive and negative feedback in Section 2.

In this paper, we focus on the case of M.O., a peculiar star forming object located at a redshift of $z = 0.0189$ (C06) that is currently being bombarded by a FR I radio jet from the nearby galaxy NGC 541. The M.O. system is of particular interest due to the lack of evidence for an especially dense ISM or IGM. There is also not much evidence for cold gas outside of the jet interaction site as is the case in Centaurus A. As a result, it is unlikely that significant star formation would proceed in M.O. without the interaction of the jet.

A strong argument in favor of jet-induced star formation in M.O. is the morphology of the jet-cloud interaction site. Outside of the jet interaction, the gas in M.O. is warm ($\sim 10^4$ K) and clumpy. Near the jet interaction site there is a double structure of H I gas wrapped around the jet and numerous H₂ regions (C06). C06 thus determined that it is likely that the jet interaction in M.O. caused the warm gas to cool into the H₂ regions straddling the jet, in contrast to the pre-existing cold gas regions in Centaurus A. Also, the star forming regions in M.O. correlate with the jet-cloud morphology; the region where the star formation is the highest is the center of the jet-cloud interaction, and the star formation rate (SFR) decreases laterally from this point (C06). Unless M.O. happens to be a very unique system, then it may be that jet-induced star formation is a more general phenomenon than previously thought.

The present work can be viewed as an extension of our earlier study of the interactions of radiative shocks with clouds (Fragile et al. 2004). That work focused mostly on the effects of planar shocks overtaking individual (or small collections of) warm clumps on the scale of ~ 100 pc. In the current work, we explore the much richer problem of a full jet intersecting an inhomogeneous intergalactic cloud on the scale of tens of kpc. The paper proceeds as follows: Section 2 covers the theory behind jet-cloud interactions, Section 3 describes the numerical models used to capture the M.O. system, Section 4 details the simulation results, and Section 5 concludes the findings.

2. JET-CLOUD INTERACTIONS

The basic idea of jet-induced star formation (i.e. positive feedback) is that the collision of the jet with the cloud will trigger a series of shocks within the cloud. The immediate effect of these shocks will be to compress and heat the gas. Depending on how the radiative processes scale with density and temperature, the net result can be to dramatically increase the radiative efficiency within the cloud. If the temperature dependence is shallower than the density dependence, the cloud can enter a phase of runaway cooling. This process occurs most quickly in relatively over-dense regions of the original cloud. These over-dense regions then proceed to collapse at an accelerating pace. Provided some of these clumps start sufficiently close to the Jeans limit, this collapse will push them beyond this limit, such that gravitational collapse can take over and the clump will proceed to form stars.

The properties of the jet and cloud are key to controlling this process. For positive feedback to be important, the initial cloud must be dense enough for some parts to be reasonably close to the Jeans limit. The temperature must also be such that any increase in temperature is met with a dramatic increase in cooling (the hydrogen cooling edge at $\sim 10^4$ K is a good example). It generally helps for the jet to be significantly less dense than the cloud. Finally, the jet velocity needs to be fast enough to trigger shocks in the cloud, yet not so fast that the cloud is disrupted before cooling can have much of an effect.

3. NUMERICAL MODELS

Our numerical simulations are performed using the well-tested *Cosmos++* computational astrophysics code (Anninos et al. 2005), specifically its Newtonian hydrodynamics solvers. *Cosmos++* carries over many of the multi-physics capabilities found in its predecessor code *Cosmos* (Anninos et al. 2003). The Newtonian solvers have previously been utilized to study the bar mode instability in magnetized, rotating neutron stars (Camarda et al. 2009) and the galactic center G2 event (Anninos et al. 2012). The current work uses the High Resolution Shock Capturing (HRSC) scheme, which was described in its relativistic form in Fragile et al. (2012). As there are few differences between the relativistic and Newtonian forms, we do not give a full presentation here, focusing instead on the packages that are most important to this paper: chemistry, cooling, and star formation. Note that, although magnetic fields can play an important role in shock-induced star formation (cf. Fragile et al. 2005), they are not considered in this work.

Most prior numerical studies of stimulated star formation from jet-generated shocks have been hampered by the

resolution of the computational mesh (e.g. [Fragile et al. 2004](#)). In the present work, we significantly improve on previous resolution limitations by employing the adaptive mesh refinement (AMR) capabilities of *Cosmos++*. *Cosmos++* employs a *local* AMR scheme, in which refinement and de-refinement decisions are made on a cell-by-cell basis, using an oct-tree network to traverse the grid hierarchy. Each level of refinement doubles the spatial resolution in each dimension within a given parent cell. This style of local AMR scheme ensures that the refinement and de-refinement conform as closely as possible to the shape of the region of interest, in this case the shocks and unstable cooling fronts triggered inside the cloud by the jet.

In this work, we present an idealized case of a direct, axially symmetric collision between a jet and a pre-existing spherical cloud. As such, it is a simple, and well controlled, test simulation, though its correspondence with M.O. is imperfect. In the case of M.O., it is thought that the collision was between a jet and a stellar bridge connecting the elliptical galaxy, NGC 541, with the interacting galaxies, NGC 545/547 (C06). There is also evidence that the jet is slowly sweeping across M.O. (C06). Despite these differences, the correspondence in parameters between our simulation and M.O. ensure that our results are applicable and the simulation can be used to better understand the dynamics of this particular object and of jet-induced star formation more generally.

3.1. Simulation Setup

Although we performed some two-dimensional simulations to test different code options and explore our parameter space, we mostly focus on reporting the results of our 3D simulations. The 3D simulations have a base resolution of either $288 \times 96 \times 96$ or $384 \times 128 \times 128$ zones to cover a domain that is approximately $30 \text{ kpc} \times 10 \text{ kpc} \times 10 \text{ kpc}$ with reflection boundaries applied in the y - and z -directions, so that we only simulate one quadrant of the full problem. The finest spatial resolution achieved is 19.5 pc per zone, reached by including 2 levels of refinement on top of the $384 \times 128 \times 128$ base mesh, equivalent to a uniform mesh of $1536 \times 512 \times 512$ zones. The criterion used for refinement is that any zone with $n \geq 0.1 \text{ cm}^{-3}$ is kept at the maximum refinement, while zones that fall below $n < 0.05 \text{ cm}^{-3}$ are allowed to de-refine, provided neighboring zones never differ by more than one level of refinement and no zone is allowed to drop below the base resolution. Zones are checked against the refinement and de-refinement criteria once every ten evolution steps in the numerical code. We find that a minimum resolution close to our base value is required even in the background in order to get reasonable convergence in the star formation rate (as will be discussed in Section 4.4).

The cloud, which represents the parent object of M.O., is initialized with a radius of $r_c = 7500 \text{ pc}$. It is, therefore, somewhat smaller, in terms of projected area, than the real value of 275 kpc^2 (C06). The gas within the cloud is distributed using a random, log-normal density, $n_{\text{cl}} = e^{\mu + \sigma X} e^{-5r/r_c} \text{ cm}^{-3}$, with mean and median values of $e^{\mu + \sigma^2/2} = 1.65 \text{ cm}^{-3}$ and $e^\mu = 1.0 \text{ cm}^{-3}$, respectively, where X is a randomly drawn variable with a mean of 0 and variance of 1. The gas has a mean molecular weight of $\mu = 0.62$, appropriate for approximately solar metallicity gas. The total mass of our cloud ends up being $2.2 \times 10^9 M_\odot$, about a factor of four more than the estimated H I mass of M.O. ($4.9 \times 10^8 M_\odot$; C06).

The cloud is immersed in a background gas with $n_b = 5 \times 10^{-4} \text{ cm}^{-3}$ and $T_b = 1.15 \times 10^7 \text{ K}$. The cloud and the background are initially assumed to be in pressure equilibrium, which is used to set the initial temperature of the cloud. This gives a value around $T_{\text{cl}} \approx 10^4 \text{ K}$. Each simulation is run for five sound-crossing-times, r_c/c_s , of the cloud, which corresponds to about 73 Myr total. To avoid numerical problems caused by the background gas density dropping too far below its initial value, we set a density floor of 10^{-7} cm^{-3} .

A jet is introduced into the simulation domain through one end. For this work, we choose $n_{\text{jet}} = 5 \times 10^{-6} \text{ cm}^{-3}$ (with μ the same as the cloud), a jet diameter of $D_{\text{jet}} = 1500 \text{ pc}$, and a jet velocity of 10% of the speed of light. For a cylindrical jet, this yields a kinetic power, $P_{\text{jet}} = \rho_{\text{jet}} A_{\text{jet}} v_{\text{jet}}^3 = 2 \times 10^{42} \text{ erg s}^{-1}$, where A_{jet} is the cross-sectional area of the jet. Our dependence on these model parameters is explored in Section 4.5.

3.2. Chemistry Models

In our simulations, we follow the abundances of 9 atomic and molecular species: H I, H II, He I, He II, He III, e^- , H^- , H_2 , and H_2^+ . The evolution of each species is governed by equations of the form

$$\frac{\partial \rho^{[m]}}{\partial t} + \nabla \cdot (\rho^{[m]} \mathbf{v}) = \sum_{i=1}^{N_s} \sum_{j=1}^{N_s} k_{ij}(T) \rho^{[i]} \rho^{[j]} + \sum_{i=1}^{N_s} I_i(\nu) \rho^{[i]}. \quad (1)$$

These rate equations are solved using a stable, semi-implicit, backward difference scheme that we developed in [Anninos et al. \(1997\)](#), and which has since become a standard method adopted by the general community (e.g. [Smith et al.](#)

2016) due to its combination of robustness, efficiency, and accuracy. A total of 27 gas-phase chemical reactions are included in the full network (k_{ij}), including 19 collisional and 8 photoionization/photodissociation processes. The exact reaction chains are spelled out in Anninos et al. (2003). The photoionization field is $10^{-21}(\nu/13.6 \text{ eV})^{-1.5} \text{ s}^{-1}$, appropriate for cosmic UV background radiation at low redshift (Bechtold et al. 1987). The photodissociation rate is $5.0 \times 10^{-11} \text{ s}^{-1}$, appropriate for the local interstellar medium (Spaans & Neufeld 1997).

3.3. Cooling Models

The energy equation

$$\frac{\partial E}{\partial t} + \nabla \cdot [(E + P)\mathbf{v}] = -\Lambda(T, n^{[m]}) , \quad (2)$$

where $E = e + \rho v^2/2$ is the total energy density, including the internal and kinetic contributions, accounts for the cooling and heating of the gas via a total of seven different mechanisms: collisional-excitation, collisional-ionization, recombination, bremsstrahlung, metal-line cooling (dominantly carbon, oxygen, neon, and iron), molecular-hydrogen cooling, and photoionization heating. The cumulative cooling function is

$$\Lambda(T, n^{[m]}) = \sum_{i=1}^{N_s} \sum_{j=1}^{N_s} \dot{e}_{ij}(T) n^{[i]} n^{[j]} - \sum_{i=1}^{N_s} J_i n^{[i]} + \dot{e}_M(T) n^2 , \quad (3)$$

where $\dot{e}_{ij}(T)$ are the cooling rates from 2-body interactions between species i and j and J_i represents the frequency-integrated photoionization and photodissociation heating rates. \dot{e}_M is the temperature-dependent cooling rate for metals (including carbon, oxygen, neon, and iron lines, assuming solar metallicity), taken from Dalgarno & McCray (1972). A cooling floor is set at $T_{\text{floor}} = 100 \text{ K}$, below which only adiabatic cooling is possible. In practice, we rarely see temperatures below $\sim 10^3 \text{ K}$.

3.4. Star Formation Model

In this study, we are particularly interested in tracking the formation of stars within the cloud. We follow the approach of Raseria & Teyssier (2006) in defining a density threshold, n_* , above which star formation is triggered at a rate given by

$$\dot{\rho}_* = \frac{\epsilon \rho}{t_{\text{ff}}} \quad (4)$$

where $t_{\text{ff}} = \sqrt{3\pi/32G\rho}$ is the local free-fall time and ϵ controls the star formation efficiency. We use values $n_* = 4 \text{ cm}^{-3}$ and $\epsilon = 0.1$ for most of this work, though in Section 4.4 we explore how these choices affect our results. This star formation appears as a sink term in the continuity equation

$$\frac{\partial \rho}{\partial t} + \nabla \cdot (\rho \mathbf{v}) = -\dot{\rho}_* . \quad (5)$$

By tracking how much mass is lost to star formation during each compute cycle, we are able to continuously track the star formation rate throughout the simulation.

We track the most massive ($M_* \geq 0.01 M_\odot$) “stars” created in this way using tracer particles. Each star particle is given an initial velocity equal to the velocity of the gas in the zone in which the star is created. Each star particle’s velocity remains constant for the remainder of the simulation, as these particles are not acted on by any force. This is not entirely realistic as some momentum may get redistributed during the free-fall process that leads to star formation. On longer timescales, gravitational forces from the rest of the cloud will also act on the stars, eventually altering their velocities. These effects are not considered in this work.

At the temperatures typical of star formation in our simulations ($T_* \approx 9000 \text{ K}$), the Jeans length is

$$R_J = \left(\frac{15kT}{4\pi G \mu m_H \rho} \right)^{1/2} \approx 700 \text{ pc}, \quad (6)$$

which is considerably less than the radius of the cloud, yet well above the resolution limits of our simulations. However, since self-gravity is not included in our current simulations, the clumps can not truly become Jeans unstable.

4. RESULTS

Table 4 summarizes the 15 simulations presented in this work. The naming convention refers to the base resolution and how many total grid resolution levels there are. Figure 1 presents a volume visualization from the end time of our

Table 1. Jet-Cloud Models and Parameters

Name	Resolution ^a	N_l ^b	n_* (cm^{-3})	ϵ	D_{jet} (kpc)	v_{jet} (c)	ρ_{jet} (10^{-6} cm^{-3})
288x96_2level	288×96	2	4	0.1	1.5	0.1	5
288x96_3level	288×96	3	4	0.1	1.5	0.1	5
288x96_4level	288×96	4	4	0.1	1.5	0.1	5
288x96_5level	288×96	5	4	0.1	1.5	0.1	5
288x96_3level_n1.e.05	288×96	3	1	0.05	1.5	0.1	5
288x96_3level_n4.e.05	288×96	3	4	0.05	1.5	0.1	5
288x96_3level_n7.e.05	288×96	3	7	0.05	1.5	0.1	5
288x96_3level_rhoj10	288×96	3	4	0.1	1.5	0.1	50
288x96_3level_Dj2	288×96	3	4	0.1	3.0	0.1	5
288x96_3level_vj5	288×96	3	4	0.1	1.5	0.5	5
384x128_3level	384×128	3	4	0.1	1.5	0.1	5
288x96x96_2level	$288 \times 96 \times 96$	2	4	0.1	1.5	0.1	5
288x96x96_3level	$288 \times 96 \times 96$	3	4	0.1	1.5	0.1	5
384x128x128_2level	$384 \times 128 \times 128$	2	4	0.1	1.5	0.1	5
384x128x128_3level	$384 \times 128 \times 128$	3	4	0.1	1.5	0.1	5

^aResolution refers to the base resolution.

^b N_l is the total number of grid refinement levels.

highest resolution 3D simulation (384x128x128_3level). A number of general features are apparent. First, the cloud is dense enough and has enough inertia to dramatically slow the propagation of the jet (represented by its temperature in red). At the speed the jet is traveling, if not for the cloud (and, to a lesser extent, the background gas) impeding its progress, it should have traversed 74.6 box lengths (298.4 cloud radii) over the duration of the simulation. Instead, most of the jet material is deflected to the sides of the cloud, though a significant fraction of its energy is deposited within the cloud gas. The green material represents neutral hydrogen (H I) and shows that the core of the original cloud remains relatively intact. Some cooling (represented by the blue, H_2 , gas) is happening on the fringes of the cloud (at a radius of about $0.5r_c$ in Figure 1), where weak shocks are being driven into the cloud by what is effectively now an over-pressure cocoon around the cloud. More substantial cooling is happening toward the front of the cloud in the post-shock gas (dense blue filament just downstream of where the jet terminates).

Figure 2 shows what the evolution looks like in one of our 2D simulations (384x128_3level). This evolution shows broad similarities to what is seen in the 3D simulations, although there are notable differences. For one, the jet has penetrated much further into the cloud in 2D by the end of the simulation. We will also discuss in Section 4.2 how the cooling and star formation in 2D take place in a “wall” proceeding forward through the cloud, while in 3D, they take place in a ring, centered about the jet axis. In Section 4.3, we also find that the star particles have a broader velocity distribution in 2D than 3D. Such differences illustrate the necessity of 3D simulations.

4.1. Shock Propagation

Figure 3 is a volume visualization showing regions of significant velocity convergence ($\nabla \cdot \mathbf{v} < 0$), as an indicator of where shocks are located. From it, we see that, even after 73 Myr, the jet-driven shock still has not reached the center of the cloud. We can compare this plot with the estimated shock velocity in the cloud. For our chosen jet velocity, $v_{\text{jet}} = 3 \times 10^4 \text{ km s}^{-1}$, we can use the shock jump conditions,

$$v_{\text{ps}} = \left(1 - \frac{\Gamma - 1}{\Gamma + 1}\right) v_{\text{sh}} , \quad (7)$$

where v_{ps} and v_{sh} are measured in the rest frame of the pre-shock gas, to estimate the speed of the shocks in the background gas, $v_{\text{sh,b}} \approx 4v_{\text{jet}}/3 = 4 \times 10^4 \text{ km s}^{-1}$. If the shock in the background is strong, then the postshock pressure is approximately $\rho_b v_{\text{sh,b}}^2$. If we assume the shocks are also strong inside the cloud and that the postshock background and cloud gas reach pressure equilibrium, then we can estimate the speed of the shock in the cloud

$$v_{\text{sh,cl}} \simeq \left(\frac{\rho_b}{\rho_{\text{cl}}}\right)^{1/2} v_{\text{sh,b}} = \frac{v_{\text{sh,b}}}{\chi^{1/2}} . \quad (8)$$

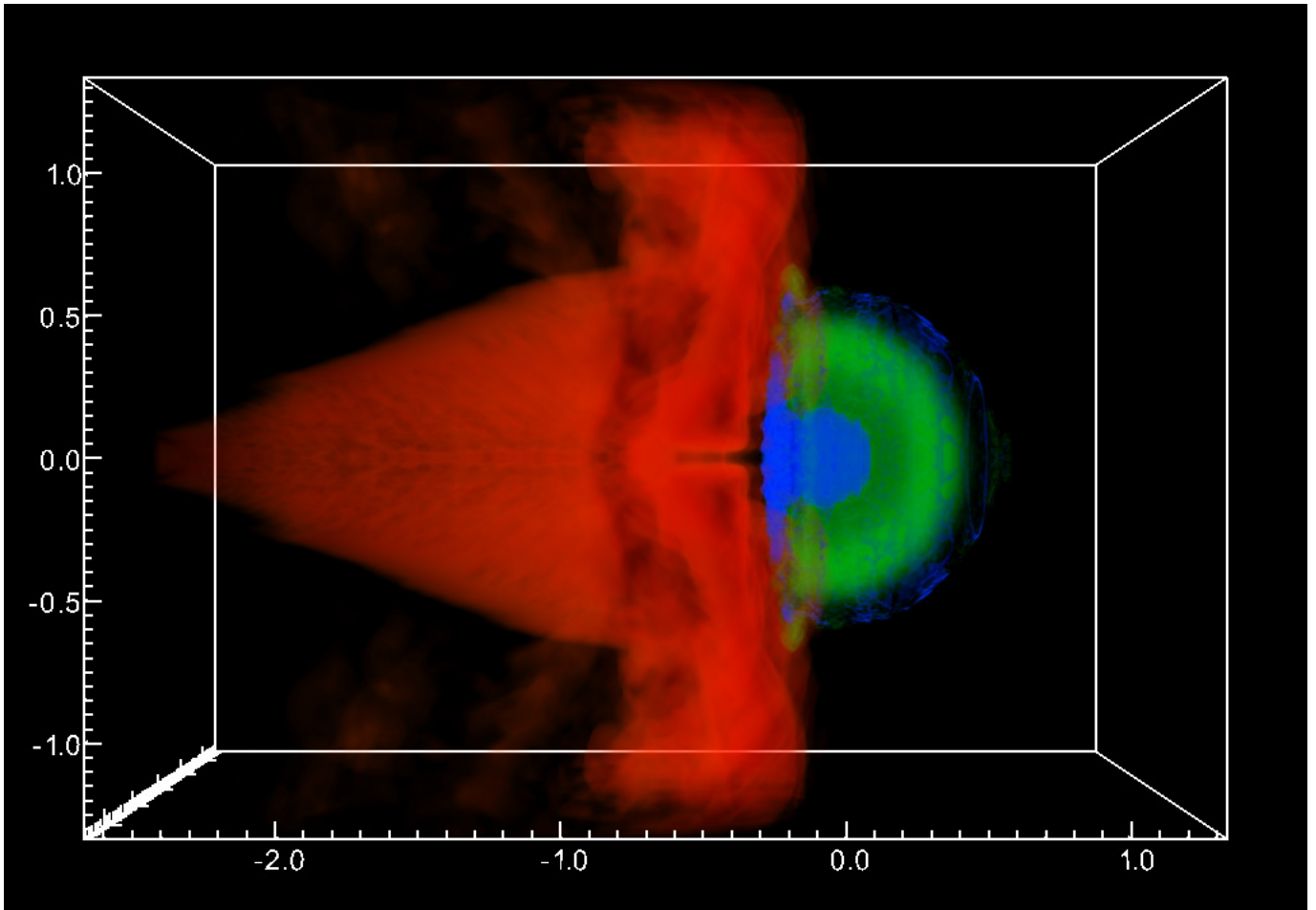


Figure 1. Volume visualization from the final time dump ($t = 73$ Myr) of our highest resolution 3D simulation (384x128x128_3level). Red represents hot, $T > 2 \times 10^8$ K, material, mostly the jet, although possibly with some cloud gas mixed in; green represents regions of the cloud with a neutral hydrogen density, $n_{\text{HI}} \sim 0.01 \text{ cm}^{-3}$; and blue represents regions of the cloud with a molecular hydrogen (our tracer for cold gas) density, $n_{\text{H}_2} \geq 10^{-8} \text{ cm}^{-3}$. Data have been reflected across the $y = 0$ and $z = 0$ planes to create this image. Axes are marked in units of cloud radii, r_c .

For our median cloud density, $n_{\text{cl}} = 1 \text{ cm}^{-3}$, this gives us a shock speed in the cloud of $v_{\text{sh,cl}} \simeq 45 \text{ km s}^{-1}$. Thus, the shock should have traveled approximately 22% of the way through the cloud by the end of our simulation, roughly consistent with Figure 3. As expected, material that is ahead of the shock (downstream) remains relatively undisturbed, except on the fringes of the cloud where the over-pressure cocoon is driving weaker shocks into the cloud (blue outline of the cloud in Figure 3).

4.2. Cooling Front

As mentioned in Section 2, for the jet feedback to be positive, it is critical for the cooling timescale to be short compared to the shock-crossing time of the cloud. Following Fragile et al. (2004), we estimate the cooling time to be

$$t_{\text{cool}} = (7.0 \times 10^{-35} \text{ g cm}^{-6} \text{ s}^{-1}) \frac{v_{\text{sh,b}}^3}{\chi^{3/2} \rho_{\text{cl}}} \simeq 200 \text{ yr}. \quad (9)$$

This is *much* shorter than any other relevant timescale in the problem.

Interestingly, the greatest amount of cooling (and associated star formation) is seen in a ring radiating away from the initial impact point at the head of the cloud. In Figure 1, you can see evidence of this in the light green ring of H I just to the left of the cloud's center. A smaller, denser ring of H₂ follows behind the H I ring. Figure 4 shows how this cooling front and associated star formation moves over the course of the simulation. This distribution is significantly different than what one sees in 2D simulations (Figure 2), where cooling and star formation occurs more uniformly

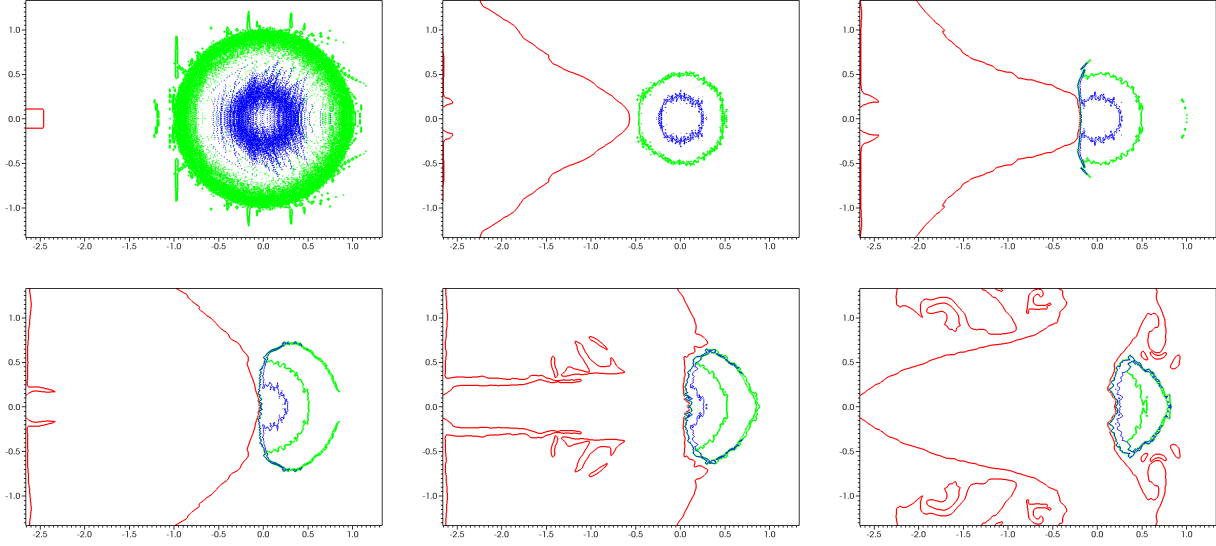


Figure 2. Contour plots from the 2D simulation 384x128_3level, with colors representing the same materials as in Fig. 1, i.e. red represents $T > 2 \times 10^8$ K, green represents $n_{\text{HI}} = 0.01 \text{ cm}^{-3}$, and blue represents $n_{\text{H}_2} = 10^{-7} \text{ cm}^{-3}$. The panels show the evolution, spaced at intervals of one cloud-crossing time, i.e. $t = \{0, 1, 2, 3, 4, 5\} r_c / c_s$. The dramatic change in the size of the cloud between the first and second panels is due to photoionization. The overall size and density of the cloud does not change much, but the ionization levels do.

across the cloud diameter (perpendicular to the jet propagation).

Figure 5 helps clarify the nature of these rings. Note first that, as expected, there is a compression front moving forward through the body of the cloud (approximately vertical feature extending from $\{-0.2, 0\}$ to $\{-0.2, 0.75\}$ in both panels). There is also a compression front moving radially into the cloud from all sides (arced feature extending from $\{-0.2, 0.6\}$ to $\{0.4, 0.6\}$ in both panels, although it extends around the entire cloud), driven by the over-pressured cocoon. Cooling seems to be operating effectively in both of these regions, as the temperature remains $\lesssim 10^4$ K (blue regions in the right panel). However, in most parts of these fronts, the density does not quite reach the threshold for star formation ($n \lesssim n_*$). This does *not* appear to be a resolution effect as the fronts are well resolved in most places and our overall S.F.R. seems to have converged (see Figure 9). Instead, the ring of star formation seen in Figures 4 and 8 seems to correspond to regions where the forward propagating compression wave intersects the radial compression front (most strongly around $\{-0.11, 0.63\}$). The combined effect of the two shocks is enough to push the density over the star formation threshold.

4.3. Star Particles

As a reminder, whenever more than $0.01 M_\odot$ of gas is converted into stars within a given zone within a single cycle, then a star particle is created to track the properties, such as position, age, and velocity, of that “star.” Following this prescription, we created over 1.2×10^7 star particles in our highest resolution simulation (384x128x128_3level). The star particles span an age range from 0 – 72 Myr, although the star particles associated with the jet interaction are all younger than about 50 Myr; the oldest stars formed spontaneously at the start of the simulation inside zones whose random density exceeded the star formation threshold. Even the 50 Myr age is considerably older than the stellar age range of 7.0-8.5 Myr estimated for M.O. (C06). Much of this discrepancy can be explained by the delay associated with the free-fall time, which is not accounted for in the “ages” of our star particles. For our threshold density, n_* , the associated free-fall time is $t_{\text{ff}} = 33$ Myr, bringing the ages more in line with M.O. Furthermore, the stellar ages in C06 may actually be telling us more about the age of the jet. It may be that M.O. has not yet evolved for as long as we ran our simulations.

An interesting point about the stellar ages in our simulations is that they show a negative curvature along the direction of jet propagation, that is, the youngest (currently forming) stars are found between two populations of slightly older stars, one in the upstream direction and one downstream. This can be seen for one of our 2D simulations in the right panel of Figure 6. The upstream population are stars that formed recently, only slightly before the current star formation. The downstream population are some of the first stars to form from the jet interaction, but they are

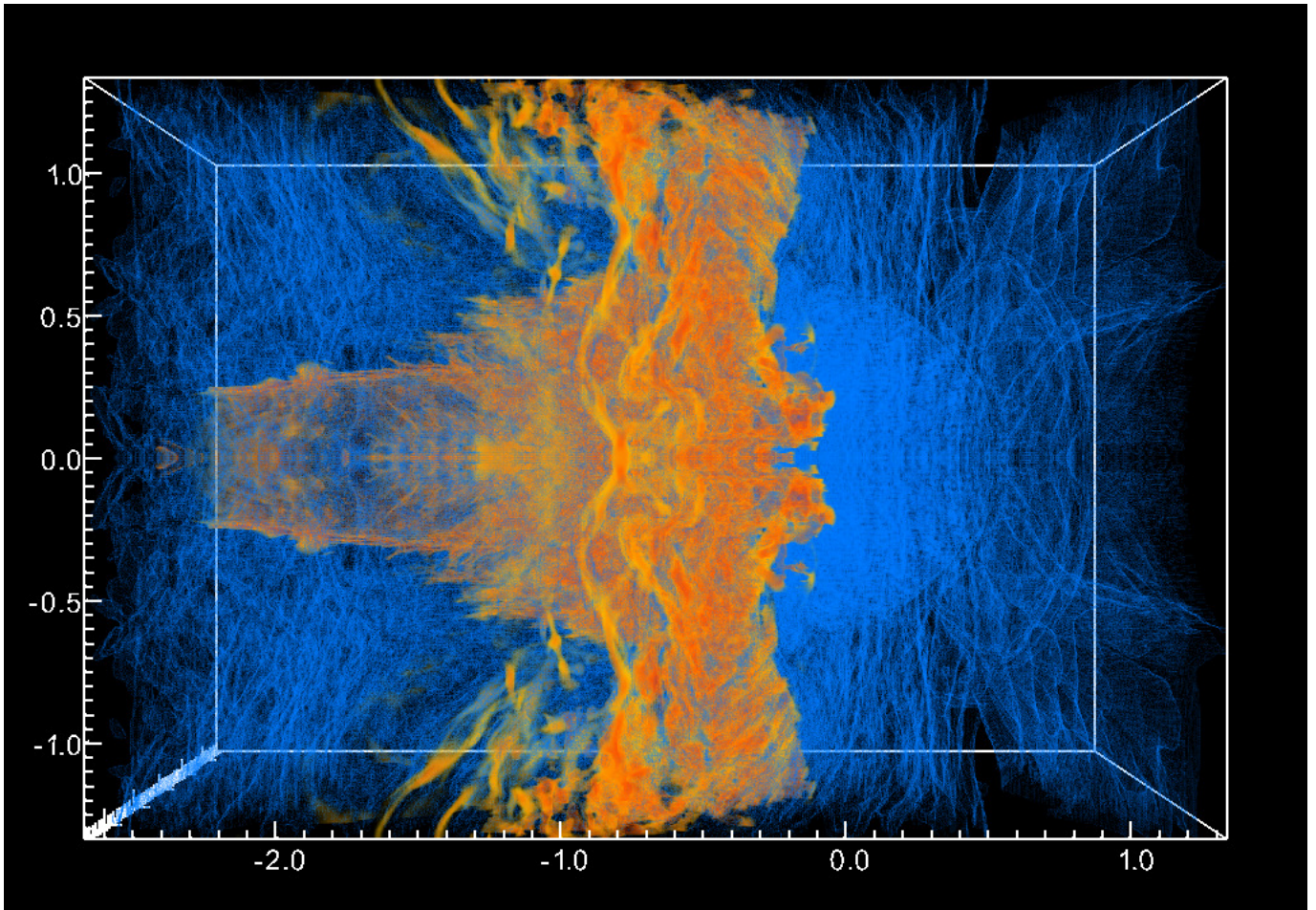


Figure 3. Volume visualization of regions of velocity convergence ($\nabla \cdot \mathbf{v} < 0$), indicative of shocks, from the final time dump ($t = 73$ Myr) of our highest resolution 3D simulation (384x128x128.3level). Yellow, orange, and red shades indicate the strong shocks associated with the jet, while blue indicates much weaker shocks. Data have been reflected across the $y = 0$ and $z = 0$ planes to create this image. Axes are marked in units of cloud radii, r_c .

now actually located ahead of the current star formation front because they received a velocity kick larger than the current shock speed. Since the star particles are not coupled to the gas, they can actually pass ahead of the shock as it slows down, giving an apparently older population ahead of the current star formation front.

By using our results from Sec. 4.1 and inverting the shock jump condition, we predict a post-shock velocity in the cloud of $v_{cl,ps} = 3v_{sh,cl}/4 \simeq 34 \text{ km s}^{-1}$, consistent with the observed 40 km s^{-1} shear velocity in M.O. (C06). Since our star particles are assigned their velocity based upon the velocity of the gas from which they form, we expect the simulated star particle velocities to be similar. Figure 7 shows a histogram of the velocity distribution of all of the star particles. The distribution peaks at around 50 km s^{-1} , which is fairly consistent with our crude predictions and the observations of M.O. Figures 6 (left panel) and 8 show the spatial distributions of the star particles, colored by the magnitude of their velocities, in 2D and 3D, respectively. Note the significant differences in the distributions, although the magnitudes of the velocities (and ages of stars) are comparable. As mentioned above, the fastest moving star particles are on the downstream edges of the distributions. They are also found further out, i.e. at larger radii, on average in the 3D simulation.

4.4. Star Formation Rate & Effects of Resolution

Figure 9 shows the measured star formation rate (S.F.R.) as a function of time for four different 3D simulations done at different effective resolutions from 57.1 pc per zone (288x96x96.2level) to 19.5 pc per zone (384x128x128.3level). As might be expected, the simulated S.F.R. is sensitive to resolution. At higher resolutions, more gas is going to be able to reach the density threshold, n_* , of our star formation model. However, at some point a limit should be reached where the high density filaments are well enough resolved that their size and peak density are no longer functions of

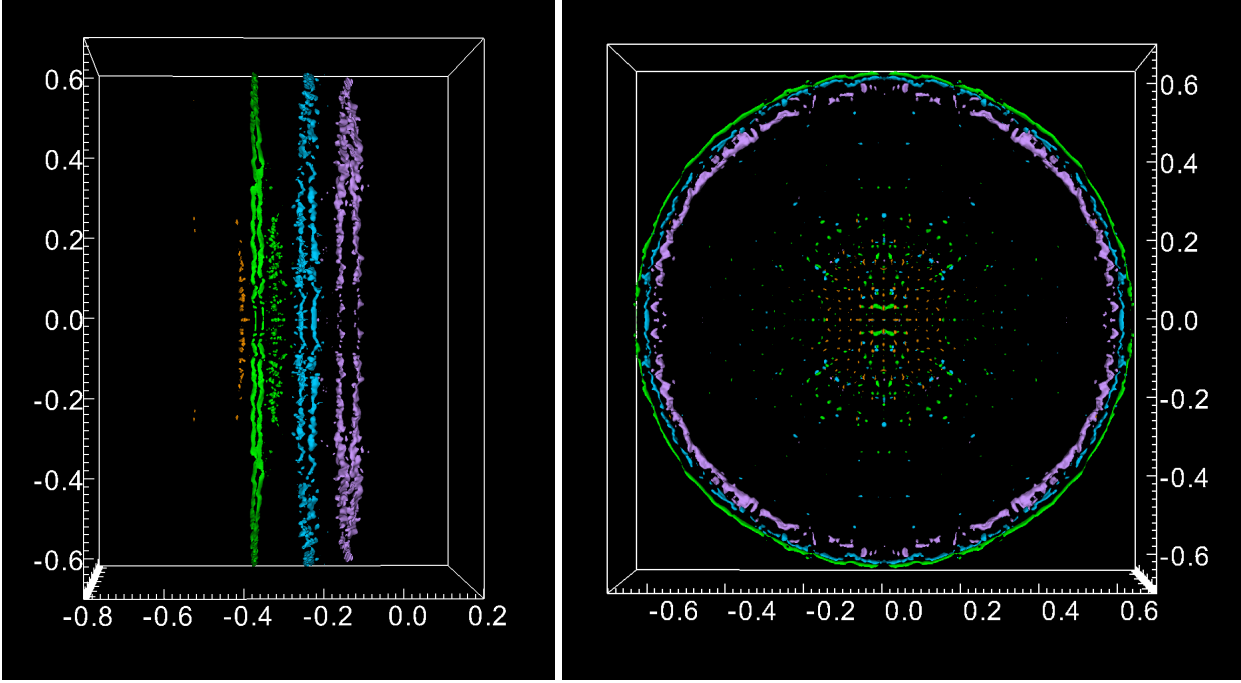


Figure 4. Isosurface plot showing regions of the simulation domain where the density exceeds the star formation limit ($n > n_*$) at $t = 29$ (orange), 44 (green), 58 (blue), and 73 Myr (purple) from our highest resolution 3D simulation (384x128x128_3level). The left panel shows a side view, while the right panel shows a head-on view. Data have again been reflected across the $y = 0$ and $z = 0$ planes.

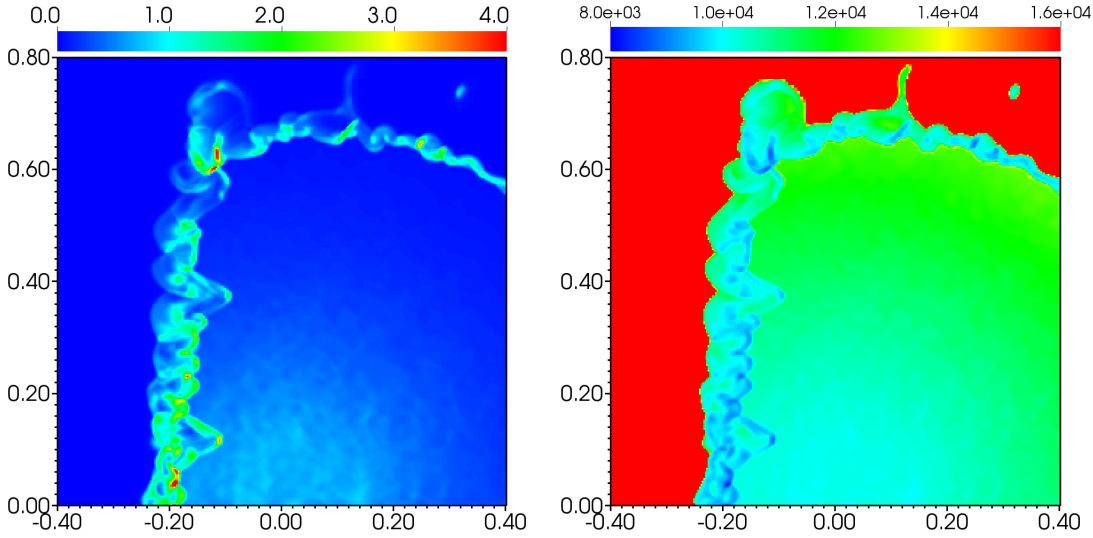


Figure 5. Two-dimensional mid-plane slices through our highest resolution 3D simulation (384x128x128_3level). As in all plots, the axes coordinates have their origin at the initial cloud center. The jet is coming from the left. The left panel shows the gas density in units of cm^{-3} . The right panel shows temperature in K. Note how the densest, coldest gas is found around $\{-0.11, 0.63\}$, where the nearly planar front moving forward through the cloud intersects the nearly spherical front being driven into the cloud.

resolution. It appears we may have reached this point in our highest resolution simulation. Note that the peak star formation rate actually goes down compared to the next lower resolution. Also, the time at which star formation begins remains consistent at about 25 Myr for the two highest resolutions. A convergence at a resolution of about 25 pc per zone also seems to be supported by our 2D tests (right panel of Figure 9), where we were able to consider even

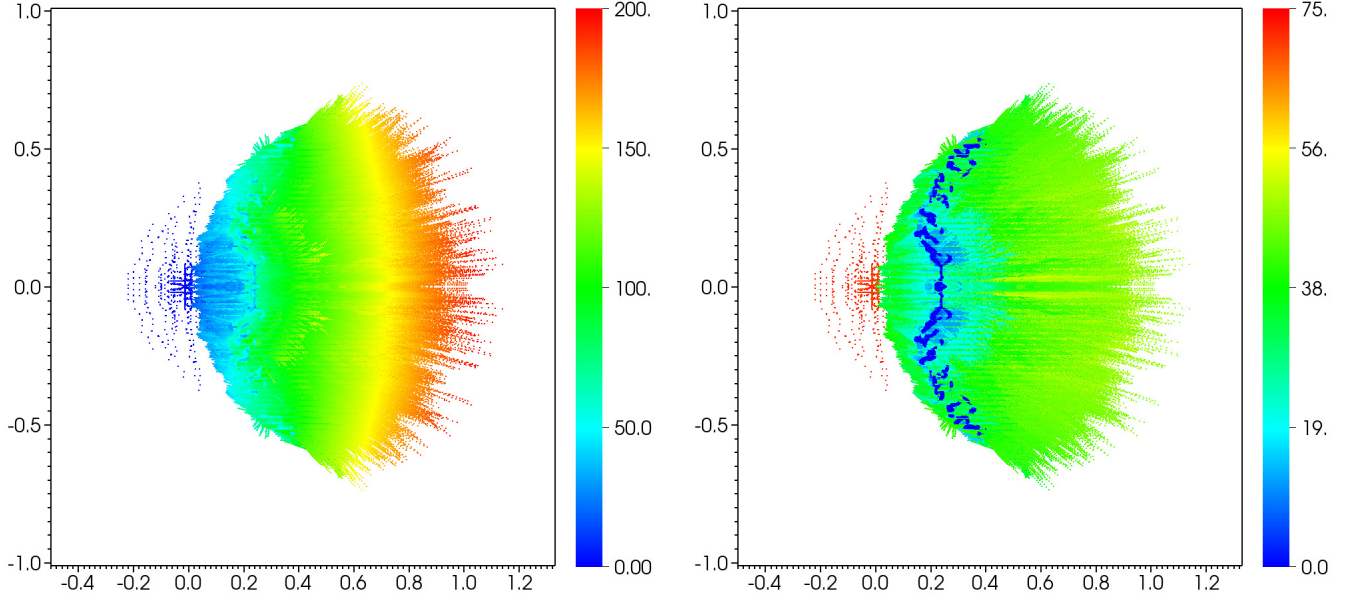


Figure 6. Plot of spatial distribution of star tracer particles from the final time dump ($t = 73$ Myr) of our 384x128_3level 2D simulation. In the left panel, the color of each particle indicates its velocity magnitude (in km s^{-1}), while in the right panel, the color indicates age (in Myr).

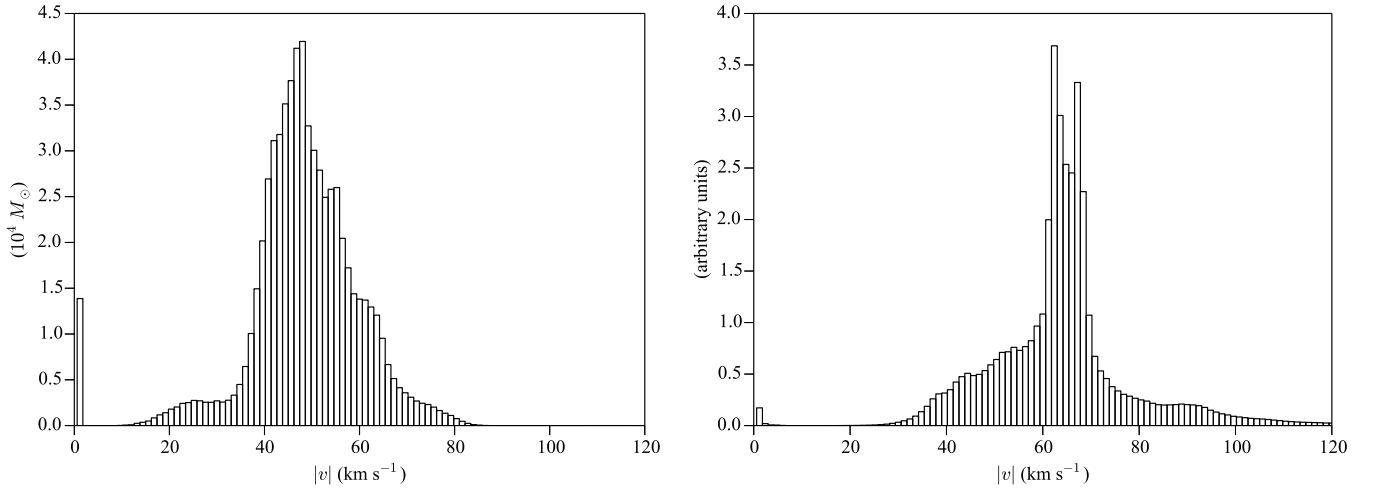


Figure 7. Histogram of the velocity magnitudes of all the star particles formed in our 384x128x128_3level 3D simulation (left) and 384x128_3level 2D simulation (right). The 0 km s^{-1} bins are filled with stars that formed in the initial cloud, prior to its interaction with the jet. The peak of the 3D distribution is roughly consistent with observations of M.O.

higher resolutions.

The S.F.R., or correspondingly the H_α luminosity, since (Kennicutt 1998)

$$\left(\frac{\text{SFR}}{M_\odot \text{ yr}^{-1}} \right) = 7.9 \times 10^{-42} \left(\frac{L_{H_\alpha}}{\text{erg s}^{-1}} \right), \quad (10)$$

in Figure 9 is about a factor of 6 less than the observed value in M.O. ($\text{S.F.R.} = 0.52 M_\odot \text{ yr}^{-1}$ and $L_{H_\alpha} = 6.6 \times 10^{40} \text{ erg s}^{-1}$; C06). This most likely means that one or more of our simulation parameters does not match the situation in M.O. To increase the S.F.R. in the simulation, we could: decrease the star formation density threshold, n_* ; increase the star formation efficiency, ϵ ; increase the jet power; or increase the initial cloud density. We use a set of 2D simulations

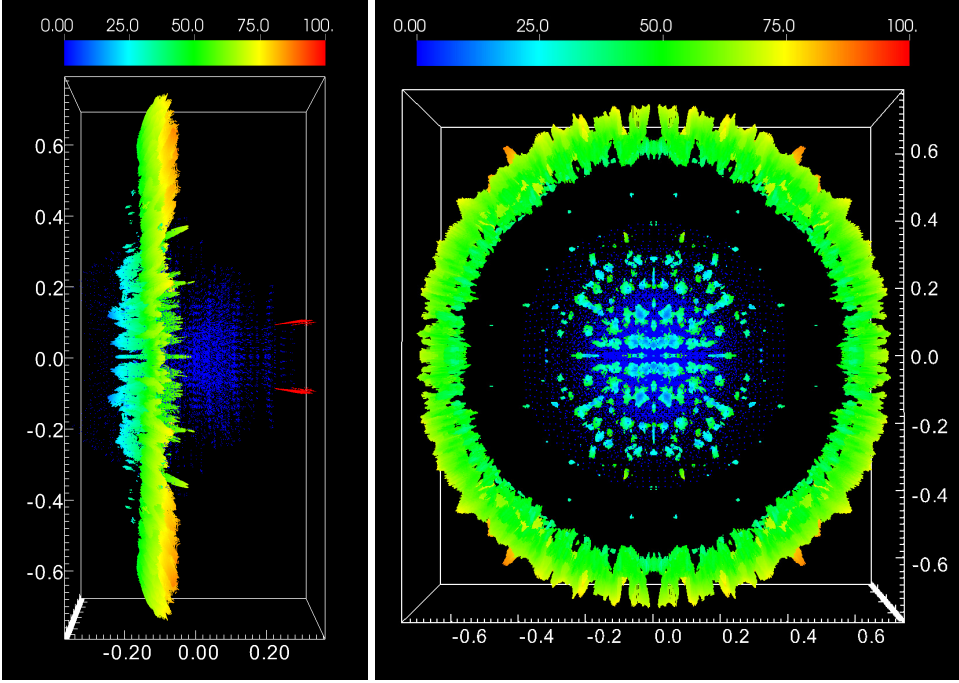


Figure 8. Plot of spatial distribution of star tracer particles from the final time dump ($t = 73$ Myr) of our highest resolution 3D simulation (384x128x128_3level). The color of each particle indicates its velocity magnitude (in km s^{-1}). The left panel shows a side view, while the right panel shows a head-on view. Data have again been reflected across the $y = 0$ and $z = 0$ planes.

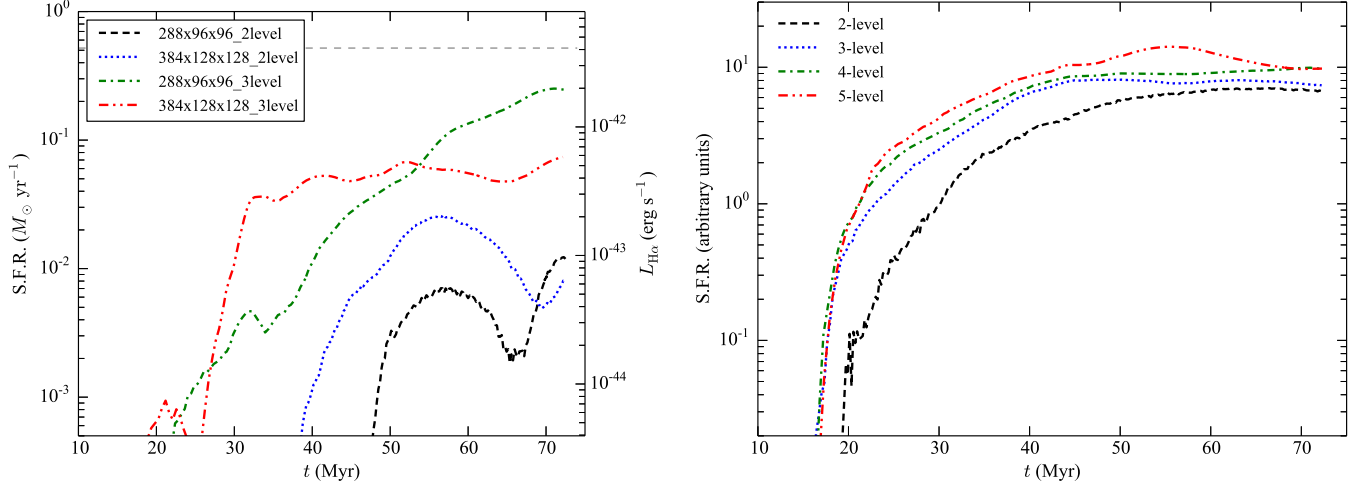


Figure 9. Star formation rate history for all of the 3D (left panel) and some 2D (right panel) simulations. All of the 2D simulations have a base resolution of 288×96 . Together, the figures suggest that our results are reasonably well converged at resolutions above about 25 pc per zone. Note that the highest resolution 3D simulation produces a steady S.F.R. of $\sim 0.07 M_{\odot} \text{ yr}^{-1}$ (corresponding to an $\text{H}\alpha$ luminosity of $5 \times 10^{-43} \text{ erg s}^{-1}$). This falls short of the observed rate in M.O. (grey, dashed line) by about a factor of 6. The units on the S.F.R. axis in 2D are arbitrary because there is no meaningful way to assign a volume to the cloud.

to test the impact of changing n_{\star} , ϵ , and the jet power. In the rest of this section, we focus on n_{\star} and ϵ . In the next section, we consider varying the parameters that affect the jet power. We do not, however, explore the effect of further increasing the cloud density, as it is already high enough to trigger spontaneous star formation. We do not want such spontaneous star formation to overwhelm the jet-induced star formation that we are studying.

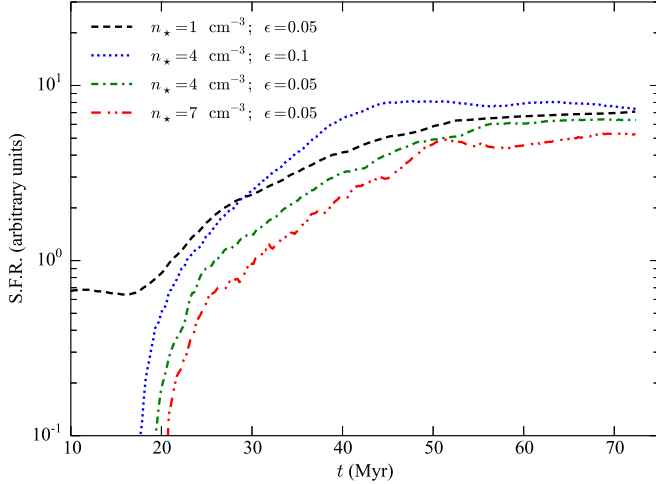


Figure 10. S.F.R. history for different values of the star formation model parameters, n_* and ϵ , for 2D simulations with a base resolution of 288×96 and 3 total resolution levels. The dotted, blue curve shows results with our default parameters. The units on the S.F.R. axis are arbitrary because in 2D, there is no meaningful way to assign a volume to the cloud.

Figure 10 shows the measured S.F.R. for four different 2D simulations using different values for n_* and ϵ . Not surprisingly, if we lower the star formation threshold density (black, dashed curve), then star formation occurs much more easily, so much so that the rate of spontaneous star formation (that not associated with the jet interaction) is within a factor of 10 of the jet-induced rate. Interestingly, cutting the star formation efficiency in half (green, dot-dashed curve vs. blue, dotted curve) does not simply cut the S.F.R. in half. This illustrates the non-linearity of this star formation process and the need for high fidelity simulations.

Ultimately, we find that adjusting the star formation parameters does not really aid in raising our measured S.F.R. Our standard parameters, $n_* = 4 \text{ cm}^{-3}$ and $\epsilon = 0.1$, already produce the highest induced S.F.R. of any of these simulations. Increasing the star formation efficiency further might yield some further increase in the S.F.R., but we are already at what we consider a reasonable upper limit.

4.5. Jet Power

Using the known correlation between jet power and radio luminosity, $P_{\text{jet}} \approx 7.2 \times 10^{36} (L_{\text{rad}}/10^{30} \text{ erg s}^{-1})^{12/17} \text{ erg s}^{-1}$ (Körding et al. 2008), and the radio luminosity of NGC 541, $L_{\text{rad}} \approx 10^{41} \text{ erg s}^{-1}$ (van Breugel et al. 1985), we estimate the kinetic power of the jet impacting M.O. to be $4 \times 10^{44} \text{ erg s}^{-1}$. By contrast, our default jet parameters give a power that is more than two orders of magnitude lower. In Figure 11, we explore how increasing the jet power would impact our results. Increasing the jet density (black, dashed curve) increases the S.F.R. and also causes star formation to start earlier. This is because a denser jet more easily penetrates the background gas to reach the cloud. Increasing the jet diameter (green, dot-dashed curve) also increases the S.F.R., although this happens gradually, not even peaking by the end of the simulation. Finally, increasing the jet velocity (red, double-dot-dashed curve) again causes star formation to start earlier, but also makes the shock crossing time comparable to the cooling timescale, such that the cloud is disrupted (and ultimately blown off the simulation domain) before a significant number of stars can form (S.F.R. goes to zero around $t = 34 \text{ Myr}$).

From these tests, it appears that the best option for matching the S.F.R. in M.O. would be a simulation with a denser jet. Extrapolating from our 2D results, and assuming the same increase is seen in 3D, it appears that a factor of 25 increase in jet density might be enough to have the peak S.F.R. in our simulation match the currently observed value in M.O. This would also bring the kinetic power of our jet more in line.

4.6. Other Comparisons with Observations

Figure 12 tracks the total mass of H I, H_2 , and stars over the course of our highest resolution simulation. While the simulation produces roughly the correct amount of H I [$3.6 \times 10^8 M_\odot$ in the simulation vs. $4.9 \times 10^8 M_\odot$ for M.O. (C06)], it produces far less H_2 [$1.1 \times 10^3 M_\odot$ vs. $\sim 10^8 M_\odot$ in M.O. (Lacy et al., in prep.)], and about a factor of 10 fewer stars [$2.2 \times 10^6 M_\odot$ vs. $1.9 \times 10^7 M_\odot$ in M.O. (C06)]. We find an electron number density in our cloud of

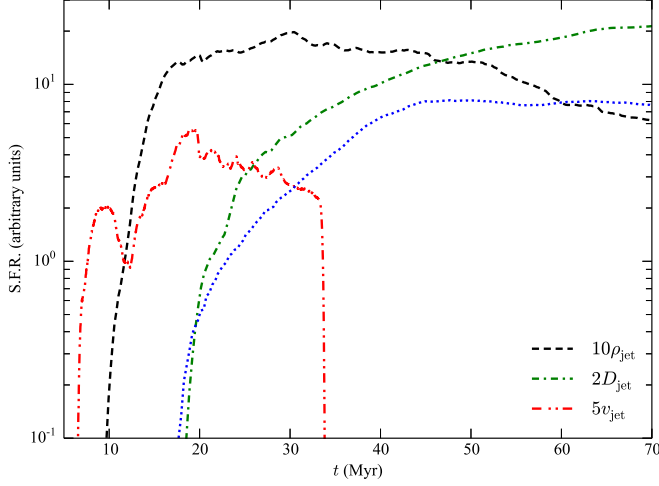


Figure 11. S.F.R. history for different values of our jet parameters, ρ_{jet} , D_{jet} , and v_{jet} , for 2D simulations with a base resolution of 288×96 and 3 total resolution levels. The dotted, blue curve shows results with our default parameters. The units on the S.F.R. axis are arbitrary because in 2D, there is no meaningful way to assign a volume to the cloud.

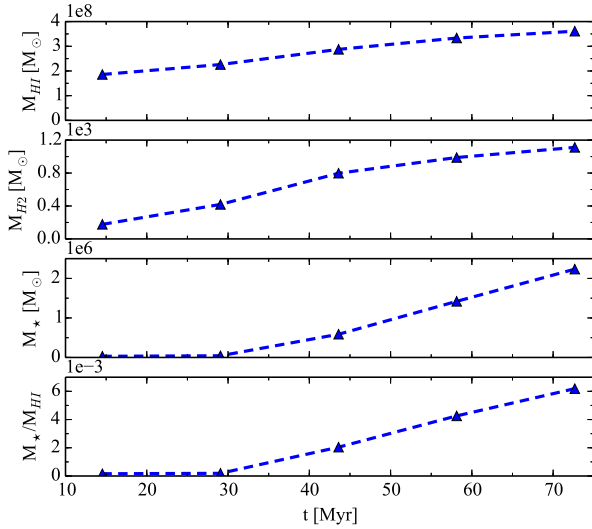


Figure 12. Plots of M_{HI} , M_{H_2} , M_{\star} , and M_{\star}/M_{HI} over time for our highest resolution 3D simulation (384x128x128_3level).

$n_e \sim 0.3 \text{ cm}^{-3}$, also somewhat lower than the range of $1\text{--}10 \text{ cm}^{-3}$ obtained for M.O. (C06). Since the amount of H I gas is comparable, this suggests that the cooling and star formation in the simulations are not nearly as efficient as they are in M.O. The sizable discrepancy in H_2 could be reduced if we included the effects of self-shielding, which would reduce the amount of photodissociation and increase the yield of H_2 . However, even in simulations where we completely ignore photodissociation, we still find the H_2 mass to be at least two orders of magnitude too low. Another important point about our H_2 values is that we are only forming H_2 through gas phase reactions. In M.O., it may be that substantial H_2 formation takes place on dust grains. However, simulations that include precipitation of H_2 on dust, with standard grain parameters, show only a very modest increase in M_{H_2} . Likely, further work will be needed to better understand the H_2 levels in M.O.

Figure 12 also tracks the “star formation efficiency,” M_{\star}/M_{HI} , over time. By this measure, our simulation achieves a peak star formation efficiency of 0.6%. This, too, is lower than the value of 4% measured in M.O. (C06). All of these discrepancies can be traced to the low S.F.R. seen in our simulations. As mentioned previously, the *peak* S.F.R. in our simulations (see Figure 9) is about a factor of 6 less than the *current* S.F.R. in M.O., though we showed in the

previous section that increasing the jet power in the simulations might be able to remove this discrepancy.

5. DISCUSSION & CONCLUSION

In this work, we use 2D and 3D simulations to model the evolution of a radio jet impacting a single, dwarf-galaxy-scale cloud in a direct, axially-symmetric collision. Our intention is to use these simulations to better understand observations of M.O., the peculiar starburst galaxy located at the termination point of the radio jet from NGC 541.

Our first, main conclusion is that jet-induced star formation (i.e. positive feedback) is possible under this scenario. Figures 9–12 all show dramatic increases in star formation attributable to the jet interaction. Interestingly, we find that most of the star formation in our 3D simulations takes place in a propagating ring centered about the jet axis (Figure 4). The ring lies at the intersection of a forward propagating shock driven into the cloud by the jet and a spherical compression shock driven by the over-pressure cocoon (Figure 5). These rings may potentially explain the torus of star formation observed in M.O. (C06). Importantly, this star formation is occurring upstream of an H I ring (compare Figures 1 and 4), also consistent with observations (C06).

Additionally, the velocity histogram of our star particles peaks at $|v| \approx 50 \text{ km s}^{-1}$ (left panel of Figure 7), which is again consistent with observations (C06). The spatial distribution of the star particle velocities is also interesting. The fastest moving star particles are found furthest downstream (Figures 6 and 8). These are also some of the first star particles to form (i.e. they are the oldest), which is consistent with a slowing of the propagation speed of the star formation front.

Despite these successes, the correlation of our results with M.O. is imperfect. The main discrepancy is that our measured star formation rate is about a factor of 6 lower than the observed value. C06 also suggested that the star formation rate in M.O. may have been even higher in the past. Along with not producing the expected mass of stars, our simulations also fall short on the amount of H_2 they produce.

In the paper, we have tried to explore possible avenues to rectify these discrepancies. We first considered our star formation model; there we found that our results are not strongly sensitive to its parameters. Further, we are already close to what we consider a reasonable upper limit for the star-formation efficiency, so there is little chance to make up the discrepancy that way.

The sensitivity of our results to the jet parameters was another matter. First, we found that the jet power may have been lower than what is inferred in the case of M.O. by as much as two orders of magnitude. In our 2D simulations, though, we found a complicated dependence of the S.F.R. on jet power (Figure 11). While increasing the jet diameter by a factor of two or the jet density by a factor of ten roughly doubled the S.F.R., increasing the jet velocity by a factor of 5 actually lowered the S.F.R. and destroyed the cloud on a relatively short timescale. A similar strong sensitivity to the shock velocity was seen in our earlier work (Fragile et al. 2004). Going the other direction and significantly lowering the jet velocity would introduce a different problem – star formation would likely proceed too slowly. Once the first generation of massive stars form, there is only a limited amount of time (of the order a few Myr) for star formation to continue before negative feedback, in the form of heating from the first massive stars, would effectively shut it off (Dong et al. 2003). This effect might explain why the S.F.R. in M.O. appears to be lower now that it was in the past – negative feedback may already be kicking in.

As future observations continue to constrain the star formation history of M.O., we plan to continue to refine our simulations. Future modifications to our setup may include: simulating non-axially-symmetric interactions between the jet and cloud; having the jet sweep across the cloud; or adding more feedback mechanisms, such as heating from young stars and supernovae.

This work used the Extreme Science and Engineering Discovery Environment (XSEDE), which is supported by National Science Foundation grant number ACI-1053575. PCF acknowledges support from National Science Foundation grants AST-1211230 and AST-1616185. JWLW acknowledges support from NRAO Student Observing Support grant SOSPA3-020. Work by PA was performed in part under the auspices of the U.S. Department of Energy by Lawrence Livermore National Laboratory under Contract DE-AC52-07NA27344.

REFERENCES

- | | |
|--|--|
| Anninos, P., Fragile, P. C., & Murray, S. D. 2003, <i>ApJS</i> , 147, 177 | Anninos, P., Zhang, Y., Abel, T., & Norman, M. L. 1997, <i>New A</i> , 2, 209 |
| Anninos, P., Fragile, P. C., & Salmonson, J. D. 2005, <i>ApJ</i> , 635, 723 | Antonuccio-Delogu, V., & Silk, J. 2008, <i>MNRAS</i> , 389, 1750 |
| Anninos, P., Fragile, P. C., Wilson, J., & Murray, S. D. 2012, <i>ApJ</i> , 759, 132 | Bechtold, J., Weymann, R. J., Lin, Z., & Malkan, M. A. 1987, <i>ApJ</i> , 315, 180 |

- Bicknell, G. V., Sutherland, R. S., van Breugel, W. J. M., et al. 2000, *ApJ*, 540, 678
- Camarda, K. D., Anninos, P., Fragile, P. C., & Font, J. A. 2009, *ApJ*, 707, 1610
- Croft, S., van Breugel, W., de Vries, W., et al. 2006, *ApJ*, 647, 1040
- Dalgarno, A., & McCray, R. A. 1972, *ARA&A*, 10, 375
- Dong, S., Lin, D. N. C., & Murray, S. D. 2003, *ApJ*, 596, 930
- Fanaroff, B. L., & Riley, J. M. 1974, *MNRAS*, 167, 31P
- Fragile, P. C., Anninos, P., Gustafson, K., & Murray, S. D. 2005, *ApJ*, 619, 327
- Fragile, P. C., Gillespie, A., Monahan, T., Rodriguez, M., & Anninos, P. 2012, *ApJS*, 201, 9
- Fragile, P. C., Murray, S. D., Anninos, P., & van Breugel, W. 2004, *ApJ*, 604, 74
- Gaibler, V., Khochfar, S., Krause, M., & Silk, J. 2012, *MNRAS*, 425, 438
- Guillard, P., Boulanger, F., Lehnert, M. D., et al. 2015, *A&A*, 574, A32
- Kennicutt, Jr., R. C. 1998, *ApJ*, 498, 541
- Körding, E. G., Jester, S., & Fender, R. 2008, *MNRAS*, 383, 277
- Nesvadba, N. P. H., Boulanger, F., Salomé, P., et al. 2010, *A&A*, 521, A65
- Ogle, P., Antonucci, R., Appleton, P. N., & Whysong, D. 2007, *ApJ*, 668, 699
- Rasera, Y., & Teyssier, R. 2006, *A&A*, 445, 1
- Salomé, Q., Salomé, P., Combes, F., & Hamer, S. 2016, *A&A*, 595, A65
- Smith, B. D., Bryan, G. L., Glover, S. C. O., et al. 2016, *ArXiv e-prints*, arXiv:1610.09591
- Spaans, M., & Neufeld, D. A. 1997, *ApJ*, 484, 785
- Sutherland, R. S., & Bicknell, G. V. 2007, *ApJS*, 173, 37
- van Breugel, W., Filippenko, A. V., Heckman, T., & Miley, G. 1985, *ApJ*, 293, 83